



1 **Potential modulation of Indian Ocean basin mode on the**
2 **interdecadal variations of summer precipitation over the East**
3 **Asian monsoon boundary zone**

4
5 Jing Wang^{1,*}, Yanju Liu², Fei Cheng^{3,*}, Chengyu Song⁴, Qiaoping Li⁵, Yihui Ding², Xiangde Xu⁶

6 ¹Tianjin Key Laboratory for Oceanic Meteorology, and Tianjin Institute of Meteorological Science, Tianjin, China

7 ²National Climate Center, China Meteorological Administration, Beijing, China

8 ³Ningbo Meteorological Observatory, Ningbo, China

9 ⁴Heilongjiang Climate Centre, Harbin, China

10 ⁵CMA Earth System Modelling and Prediction Centre, Beijing, China

11 ⁶State Key Laboratory of Severe Weather, Chinese Academy of Meteorological Sciences, Beijing, China

12

13 Correspondence: Yanju Liu (liuyan@cmac.gov.cn)

14 * Jing Wang and Fei Cheng contributed equally to this work.

15

16 **Abstract.** Based on long-term observational and reanalysis datasets from 1901 through 2014, this study investigates the
17 characteristics and physical causes of the interdecadal variations in the summer precipitation over the East Asian monsoon
18 boundary zone (EAMBZ). Observational evidence reveals that the EAMBZ precipitation featured prominent interdecadal
19 fluctuations, e.g., with dry summers during the periods preceding 1927, 1968–1982, and 1998–2010, and wet summers
20 during the periods of 1928–1938, 1946–1967, and 2011 onwards. Further analyses identify that the Indian Ocean basin
21 mode (IOBM) is an important oceanic modulator responsible for the interdecadal variations of the EAMBZ precipitation.
22 When the cold phase of the IOBM occurs, an anomalous cyclonic circulation is excited around the northeast corner of the
23 tropical Indian Ocean, which further induces a “north-low–south-high” meridional seesaw pattern over the Northeast
24 China–subtropical western Pacific (SWP) sector. Such seesaw pattern is conducive to the enhanced EAMBZ precipitation
25 through linking favorable environments for the transportation of water vapor from the SWP and the convergence over
26 EAMBZ at interdecadal timescales. For this reason, a physical-empirical model for the EAMBZ precipitation is developed
27 in terms of the IOBM cooling, which can well capture its interdecadal fluctuations and reflect their steady relationship.
28 The key physical pathway connecting the IOBM cooling with the interdecadal variations of the summer EAMBZ
29 precipitation is supported by the numerical results based on the large ensemble experiment and the Indian Ocean
30 pacemaker experiment. Our findings may provide new insights into the understanding of the causes of the interdecadal
31 variations in the summer EAMBZ precipitation, which may favor the long-term policy decision making for the local
32 hydrometeorological planning.

33

34 **1 Introduction**

35

36 The monsoonal airflows and mid-latitude westerlies are crucial components of the Asian climate system (Li and Zeng,
37 2002; Ding and Chan, 2005; Wang et al., 2008; Wu et al., 2012; Huang et al., 2015; Wang et al., 2017; Chen et al., 2018;
38 J. Huang et al., 2019). These two subsystems can synergistically induce regional precipitation fluctuations over
39 subtropical and mid-latitude Asia during the Northern Hemisphere (NH) late spring (May) and summer (June–August;
40 JJA) (Qian et al., 2009; Chen et al., 2021; Song et al., 2022; J. Wang et al., 2022). For example, Song et al. (2022) found
41 that May precipitation over the southeastern extension of the Tibetan Plateau (TP) features notable year-to-year variations,
42 which are physically linked to a unique interplay between the upstream mid-latitude westerlies and the Bay of Bengal
43 summer monsoon.



44
45 During the early stage of the northern summer, however, the mid-latitude NH westerlies shift poleward to the north of the
46 TP abruptly (Yeh et al., 1959; Schiemann et al., 2009). In this context, westerlies of mid-latitude synoptic disturbance and
47 southerlies of East Asian summer monsoon (EASM) collide with each other frequently over the East Asian monsoon
48 boundary zone (EAMBZ) (Qian et al., 2009; Wang et al., 2017; Chen et al., 2018; J. Huang et al., 2019; Zeng and Zhang,
49 2019; Chen et al., 2021; Q. Wang et al., 2021, 2022, 2023). EAMBZ is a transitional climate zone between the EASM-
50 controlled moist region and the westerly-dominated arid region over central Asia (Chen et al., 2010; Chen et al., 2018,
51 2021), stretching from the eastern flank of the TP to Mongolia and Northeast China [see Fig. 1 in Chen et al. (2021); also
52 see the red box in Fig. 1]. Notably, EAMBZ is a distinguished region with agrarian economy and animal husbandry, which
53 is largely susceptible to water resource variations (Ou and Qian, 2006; Lu and Jia, 2013). Nevertheless, many studies
54 reported that in the past century, the semi-arid EAMBZ underwent the most profound warming over East Asia, suffering
55 from serious aridification and a high risk of desertification (J. Huang et al., 2017, 2019, 2020). In this regard, EAMBZ is
56 deemed one of the “hotspots” highly sensitive to precipitation fluctuations (Qian et al., 2009; Lu and Jia, 2013; J. Huang
57 et al., 2019). Given that the EAMBZ is of an ecologically fragile environment with water shortage, a deep understanding
58 of the reasons for historical changes in summer EAMBZ precipitation could be a prerequisite for in situ ecological
59 improvement and socioeconomic development.

60
61 Existing studies have well documented physical mechanisms responsible for the interannual variability of summer
62 EAMBZ precipitation, highlighting the external moisture supply pathways, the modulators for the wet-dry condition
63 variations [e.g., the mid-latitude westerlies within the Asian westerly jet (AWJ), the western North Pacific (WNP)
64 subtropical high (WNPSH), and the EASM], and the remote modulation roles of large-scale teleconnected modes [e.g.,
65 Silk Road pattern (SRP)/circumglobal teleconnection (CGT) propagating along the AWJ and the Eurasian teleconnection
66 (EU)] and sea surface temperature (SST) anomaly patterns (Huang et al., 2015; Wang et al., 2017; Chen et al., 2018, 2021;
67 Zhao et al., 2019a, 2019b, 2020; Q. Wang et al., 2021, 2022, 2023). For instance, Q. Wang et al. (2022) suggested that
68 the positive EU phase is connected with a low pressure anomaly in the lower troposphere in EAMBZ and the Mongolia
69 region, thus favoring enhanced summertime precipitation over EAMBZ; and meanwhile, the CGT is positively coupled
70 with the EAMBZ precipitation, with ascending motion anomalies over EAMBZ during its positive phase. Chen et al.
71 (2021) established that the circulations (i.e., the mid-latitude westerlies and EASM) and the forcing of SST anomalies
72 (SSTAs) can collectively regulate the summer EAMBZ precipitation variability. The variability of westerlies is largely
73 modulated by the SRP and the meridional displacement of AWJ; while the EASM variability is mainly modulated by El
74 Niño-Southern Oscillation (ENSO). The synchronized effects of EASM and westerlies largely contribute to the rainfall
75 variability in EAMBZ. Zhao et al. (2019a) found that the tropical northern Atlantic SSTAs have significant impacts on
76 the August rainfall over the monsoon transitional zone in China through inducing a wavetrain over Eurasia and an
77 anomalous WNPSH.

78
79 Compared with the extensively explored interannual variability of the JJA EAMBZ precipitation, less efforts have been
80 devoted to its interdecadal variability. To understand and predict the summer EAMBZ precipitation, exploring its
81 interdecadal variations and the underlying physical causes are also critical, which are the main focus of the present study.
82 Previous studies suggested that the warm-season precipitation over many Asian areas features interdecadal fluctuations,
83 such as the southeastern TP in late spring (J. Wang et al., 2022) and East/Northeast Asia in summer (Si and Ding, 2016;
84 Zhang et al., 2018; Sun et al., 2019a; Piao et al., 2021). The oceanic interdecadal signals for these interdecadal changes
85 are also extensively investigated, highlighting the crucial modulation roles of basin-scale SST modes of Atlantic
86 multidecadal oscillation (AMO), Pacific decadal oscillation (PDO)/interdecadal Pacific oscillation (IPO), and Indian



87 Ocean basin mode (IOBM) (Si et al., 2021). Among these forcings, it is essential to emphasize the IOBM, a dominant
88 mode of SST variability in the tropical Indian Ocean (TIO) sector, which usually follows up a wintertime ENSO event
89 and persists into the summer through the capacitor effect (Klein et al., 1999; Yang et al., 2007; Xie et al., 2009). The
90 EASM is simultaneously correlated with the IOBM in boreal summer, which can be considered as a salient modulator for
91 the summer EAMBZ precipitation variability on interannual timescales (Chen et al., 2021). It is worth noting that the
92 IOBM also features a basin-scale warming/cooling at interdecadal timescales (Han et al., 2014), exerting active impacts
93 on the mid-latitude Asian climate (e.g., Wu et al., 2016; Li and Ma, 2018; Zhang et al., 2018; S. Wang et al., 2022). As
94 for the interdecadal variations of the summer EAMBZ precipitation, we hope to answer the following two questions: 1)
95 Did the JJA EAMBZ precipitation feature interdecadal variations? If so, 2) is there any intimate connection between
96 IOBM and the EAMBZ precipitation at interdecadal timescales? As such, this study shall extend previous studies by
97 exploring what extent and how the JJA IOBM modulate the concurrent EAMBZ precipitation variability at interdecadal
98 timescales, with the aim of providing a novel understanding for the rainfall variability over the mid-latitude semi-arid
99 zone in Asia. Note that we employ datasets with a centennial scale in this study [e.g., the precipitation data produced by
100 the Climatic Research Unit (CRU) and the atmospheric circulation data from the Twentieth Century Reanalysis (20CR)
101 datasets]. In comparison with the short-term datasets since the latter half of the 20th century, these long-term datasets can
102 separate the interdecadal variability of EAMBZ precipitation from the externally forced global climate change caused by
103 anthropogenic (e.g., greenhouse gases) and natural forcings (e.g., volcanic eruptions) more effectively (Wu et al., 2016),
104 which were widely used to investigate the physical causes of how internal fluctuations of the climate system modulate
105 the interdecadal variations of precipitation over Asia (e.g., Wu et al., 2016; Zhang et al., 2018; Sun et al., 2019a; Jiang et
106 al., 2021; J. Wang et al., 2022).

107
108 The remainder of this paper is arranged as follows. Section 2 describes the datasets and methods used in this study. Section
109 3 elucidates the characteristics of the interdecadal variations of summertime EAMBZ precipitation and the associated
110 background circulations, illustrates the mechanisms of how IOBM modulates the EAMBZ precipitation, and establishes
111 a linear regression model using the IOBM to predict the interdecadal precipitation anomalies over EAMBZ. Further
112 discussion and a summary of the major findings are provided in Section 4 and Section 5, respectively.

113 114 **2 Datasets and methods**

115 116 **2.1 Observational Data**

117
118 Several monthly mean observational datasets are utilized in the present study, including (1) the global land high-resolution
119 gridded CRU time series (TS) precipitation dataset version 3.26 (CRU TS3.26; spatial resolution: $0.5^{\circ} \times 0.5^{\circ}$; Harris et al.,
120 2014) for 1901–2017, (2) the Extended Reconstructed SST version 5 (ERSSTv5; spatial resolution: $2^{\circ} \times 2^{\circ}$; B. Huang et
121 al., 2017) for 1854–present derived from the National Oceanic and Atmospheric Administration (NOAA), and (3)
122 atmospheric variables derived from NOAA–Cooperative Institute for Research in Environmental Sciences (CIRES) 20CR
123 version 2c (20CRv2c; spatial resolution: $2^{\circ} \times 2^{\circ}$; Compo et al., 2011), except for the precipitation data, with 192 points in
124 longitude and 94 points in latitude, for 1851–2014. Note that all observational datasets cover the common time period of
125 1901–2014, which is the focused period in the present research.

126 127 **2.2 Rossby wave source**

128
129 Following Sardeshmukh and Hoskins (1988), the Rossby wave source (RWS) is calculated as:



130
$$RWS = -\nabla \cdot [V_{\chi}(\zeta + f)], \quad (1)$$

131 where V_{χ} is the divergent wind, ζ is the relative vorticity, and f is the planetary vorticity.

132

133 **2.3 Moisture flux and associated divergence**

134

135 The vertically integrated horizontal water vapor transport ($\langle WVT \rangle$) and associated divergence ($\langle WVT_{div} \rangle$) are

136 calculated using the following equations (Sun et al., 2019b; J. Wang et al., 2022):

137
$$\langle WVT \rangle = -\frac{1}{g} \int_{P_s}^{300} q \bar{V} dp, \quad (2)$$

138
$$\langle WVT_{div} \rangle = -\frac{1}{g} \int_{P_s}^{300} \nabla_p \cdot (q \bar{V}) dp, \quad (3)$$

139 where $\nabla_p \cdot ()$ denotes the horizontal divergence in the pressure coordinates; g is the gravitational acceleration; P_s is the
140 surface pressure; q is the specific humidity; and $\bar{V} = (u, v)$ is the horizontal wind vector (u and v represent the zonal and
141 meridional winds, respectively).

142

143 **2.4 Statistical methods**

144

145 This study focuses on interdecadal fluctuations in variables. The data are 11-year low-pass filtered by adopting a Lanczos
146 filter (Duchon, 1979) to extract the corresponding interdecadal signal. Several statistical methods are used, including
147 empirical orthogonal function (EOF) analysis, composite analysis, correlation analysis, and linear regression analysis. A
148 two-tailed Student's t test is used to evaluate the statistical significance. Considering the 11-year low-pass filtered method
149 can significantly reduce the degrees of freedom of the data, the following approximation is therefore deployed to calculate
150 the effective degrees of freedom (N^{eff}):

151
$$\frac{1}{N^{eff}} \approx \frac{1}{N} + \frac{2}{N} \sum_{j=1}^N \frac{N-j}{N} \rho_{XX}(j) \rho_{YY}(j), \quad (4)$$

152 where N is the sample size, and $\rho_{XX}(j)$ and $\rho_{YY}(j)$ are the autocorrelations of two sampled time series X and Y ,
153 respectively, at time lag j (Li et al., 2013).

154

155 In this study, we focus on the boreal summer season (JJA). All variables in observations and model simulations are
156 linearly detrended before further calculations and analyses to exclude potential impacts of long-term trends.

157

158 **2.5 Definitions**

159

160 **2.5.1 The research domain of EAMBZ**

161

162 From the long-term (1901–2014) perspective of the climatological mean state of converged $\langle WVT \rangle$ and pronounced
163 precipitation over the mid-latitude Asia, the EAMBZ (box in **Figs. 1a** and **1b**; 35°–55° N, 105°–130° E) is defined as the
164 collision and convergence zone between JJA dry westerly $\langle WVT \rangle$ and moist southwesterly $\langle WVT \rangle$ (**Fig. 1a**). As such,
165 there exist wetter conditions over the EASM-dominated part and drier conditions over the westerly-controlled part (**Fig.**
166 **1b**), suggesting the semi-arid transitional feature of EAMBZ (Xing and Wang, 2017). Our defined research domain of
167 EAMBZ largely matches the monsoon boundary zone defined by Chen et al. (2021), covering Inner Mongolia, Gansu,



168 Ningxia, Shaanxi, Shanxi, Hebei, Beijing, Tianjin, Shandong, Jilin, Liaoning, and Heilongjiang in China, as well as
169 eastern Mongolia and Korean peninsula. Note that the areal mean precipitation over EAMBZ in boreal summer is the
170 highest of the year accompanying the largest standard deviation (i.e., largest rainfall variability) (**Fig. S1**), which is the
171 focused season in the present study.

172

173 **2.5.2 Climate indices**

174

175 The IOBM index (I_{IOBM}) is defined as areal mean SSTAs over the TIO domain of 20°S–20°N, 40°E–100°E (Xie et al.,
176 2009). The IPO index is calculated using a method identical to that defined in Henley et al. (2015), that is, the difference
177 between SSTAs averaged over the central equatorial Pacific (10°S–10°N, 170°E–90°W) and the average of SSTAs in the
178 northwest (25°–45°N, 140°E–145°W) and the southwest Pacific (50°S–15°S, 150°E–160°W). In observations,
179 considering the coupled nature of IOBM and IPO at interdecadal timescales in boreal summer [cf. Fig. 2a in Wu et al.
180 (2016)], we hence remove the potential influence of the contemporaneous IPO on precipitation via eliminating the signal
181 of IPO index from the data of climate variables based on the partial regression technique, which is widely used in previous
182 studies (e.g., Dou and Wu, 2018; J. Wang et al., 2022).

183

184 **2.6 Model simulations**

185

186 To validate our proposed mechanisms of how the TIO SSTAs (i.e., IOBM-associated SSTAs) remotely modulate the
187 summer EAMBZ precipitation on interdecadal timescales, following the method of Zhang et al. (2019) and Yang et al.
188 (2020), we adopt monthly mean outputs from two experiments of the Community Earth System Model version 1 (CESM1),
189 which is a fully coupled Earth system model incorporating components of atmosphere, ocean, land, and sea ice (Hurrell
190 et al., 2013).

191

192 The first experiment is the CESM1 Large Ensemble Numerical Simulation (referred to as CESM1_LENS; Kay et al.,
193 2015). Among total 40 ensemble members in CESM1_LENS (Yang et al., 2020), we use the first 35 individual members
194 according to many previous studies (e.g., Touma et al., 2021; J. Wang et al., 2023), which were completed at the climate
195 modeling center of National Center for Atmospheric Research (NCAR). Note that all ensemble members in
196 CESM1_LENS were imposed with the same radiative forcing scenario (Taylor et al., 2012), with historical forcing for
197 1920–2005 and high-emission forcing scenario [i.e., Representative Concentration Pathway (RCP) 8.5] for 2006–2080
198 (Moss et al., 2010; Touma et al., 2021). The ensemble members were further generated with slightly differentiated
199 perturbations of atmospheric states (Kay et al., 2015; Touma et al., 2021). The second experiment is the CESM1 Indian
200 Ocean Pacemaker Ensemble Simulation (referred to as CESM1_IOPES), with 10 ensemble members (Zhang et al., 2019;
201 Yang et al., 2020). We adopt CESM1_IOPES to highlight the impact of SSTAs over the broader TIO domain (15°S–15°N,
202 African coast to 174°E). For the convenience of subsequent calculations and analyses, the African coast is designated as
203 40°E in this study, and a small change in the longitudes regarding the African coast may not affect the main results.

204

205 In light of Yang et al. (2020), by subtracting the CESM1_LENS ensemble mean from the CESM1_IOPES ensemble mean,
206 we can obtain responses of the climate system to the internal variability stemming from the time-varying TIO SSTAs,
207 distinguishing the impact of external radiative force changes from the intrinsic variability driven by TIO SSTAs. More
208 details about CESM1_LENS and CESM1_IOPES can be found in Kay et al. (2015) and Yang et al. (2020), respectively.
209 The variables employed here comprise precipitation and wind in atmosphere component of Community Atmospheric
210 Model version 5 (CAM5), with a spatial resolution of 1.25° in longitude and 0.9° in latitude; and SST in the ocean



211 component of Parallel Ocean Program version 2 (POP), with 320 grids in longitude and 384 grids in latitude. Before
212 further analyses, model outputs are interpolated at a resolution of $2^{\circ} \times 2^{\circ}$ using a bilinear interpolation method (Mastyło,
213 2013), identical to that of 20CRv2c. In the current study, we focus on the historical simulation period of 1920–2005.

214

215 Here, it is important to stress the following two points. First, although the TIO domain in CESM1_IOPES is broader than
216 that for defining I_{IOBM} , there exist highly consistent temporal variations in SSTAs between them in observations (Fig. S2)
217 and simulations (Fig. S3) at interdecadal timescales, with temporal correlation coefficients (TCCs) of 0.93 and 0.87 ($P <$
218 0.01), respectively. Second, when selecting the SSTAs over the broader TIO domain (purple box in Fig. S4) as a metric,
219 it can be found that the observed (Fig. S4a) and modelled (Fig. S4b) large and intense loadings of the positive SSTAs are
220 still concentrated around the narrower TIO domain (black box in Fig. S4). As such, it is plausible to adopt the above-
221 mentioned Indian Ocean pacemaker experiment with broader TIO SSTAs to validate our proposed mechanisms tied to
222 the interdecadal IOBM variations.

223

224 3 Results

225

226 3.1 Observed interdecadal variations of the summer precipitation over EAMBZ and related 227 background circulations

228

229 Figure 1c plots the spatial distribution of the interdecadal standard deviation of precipitation. This distribution is quite
230 similar to that of the climatology (Fig. 1b), suggesting relatively strong (weak) interdecadal precipitation fluctuations
231 over the EASM-dominated (westerly-controlled) part of the EAMBZ. Moreover, we show the first EOF mode of JJA-
232 mean EAMBZ precipitation (Fig. 1d), which accounts for 28% of the total variance and distinguishes from the remaining
233 eigenvectors according to the criterion defined by North et al. (1982). The leading EOF mode bears close resemblance to
234 the standard deviation of the EAMBZ precipitation on interdecadal timescales (Figs. 1c and 1d), with larger loadings
235 occupying the Bohai Sea and Korean peninsula and their adjoining regions. The interdecadal TCC between the principal
236 component of the EOF1 and area-averaged precipitation over the research domain of EAMBZ (35° – 55° N, 105° – 130° E)
237 [EAMBZ precipitation index (I_{EAMBZP}); Fig. 1e] is 0.93 ($P < 0.001$). The aforementioned results indicate that that our
238 defined I_{EAMBZP} can serve as a good indicator of the predominant fluctuations in the precipitation anomalies over EAMBZ
239 at interdecadal timescales. As such, from the time series of 11-year low-passed filtered I_{EAMBZP} (Fig. 1e), we can observe
240 that the summer EAMBZ precipitation delineates notable interdecadal fluctuations. For example, EAMBZ experienced
241 dry summers during the periods preceding 1927, 1968–1982, and 1998–2010, but underwent wet summers during the
242 periods of 1928–1938, 1946–1967, and 2011 onwards. These notable interdecadal fluctuations are basically consistent
243 with those suggested by Si et al. (2021).

244

245 Before examining the modulation of IOBM on the interdecadal EAMBZ precipitation fluctuations, it is essential to
246 scrutinize the JJA-mean I_{EAMBZP} -associated circulation anomalies. The highest mid-latitude positive correlation region
247 can be discerned north of the TP (38° – 46° N, 80° – 112.5° E; blue box in Fig. 2a), suggesting that the interdecadal
248 enhancement of the summer EAMBZ precipitation is intimately correlated with the acceleration of the upstream mid-
249 latitude westerlies at 400 hPa. In light of the method of Chen et al. (2021) and J. Wang et al. (2022), we correlate the
250 I_{EAMBZP} with the zonal winds averaged over the longitudinal range of EAMBZ at multiple levels (Fig. 2b) to further check
251 whether the most significant correlation occurs at 400 hPa. Evidently, on interdecadal timescales, the largest positive
252 correlation between precipitation and mid-latitude westerlies within 38° – 46° N does occur at the mid-tropospheric level
253 of 400 hPa, with a TCC of 0.46 ($P < 0.01$) between the I_{EAMBZP} and areal mean 400-hPa zonal wind (U400) over the



254 upstream westerly-dominated domain (**Fig. 2c**). Note that this correlation pattern exhibits a barotropic structure (**Fig. 2b**).
255 Additionally, we correlate the I_{EAMBZP} with the 850-hPa meridional winds (V850). The I_{EAMBZP} is positively correlated
256 with the key monsoonal southerly domain east of the TP (25° – 33° N, 102.5° – 112.5° E; green box in **Fig. 2d**), which is
257 located in the western portion of the EASM domain (Ying et al., 2023). The interdecadal correlation pattern between
258 meridional winds and the summer EAMBZ precipitation at multiple levels exhibits a baroclinic structure, with the
259 significant positive correlations confined below 500 hPa (**Fig. 2e**). Note that the strongest positive correlation is detected
260 at 850 hPa within 102.5° – 112.5° E, with a TCC of 0.63 (**Fig. 2f**; $P < 0.001$) between I_{EAMBZP} and areal mean V850 over
261 the key EASM-controlled domain (**Fig. 2d**).

262

263 **Figure 3** gives the JJA-mean I_{EAMBZP} -regressed circulation anomalies at interdecadal timescales. The interdecadal
264 enhancement of the EAMBZ precipitation is significantly linked to a localized quasi-barotropic cyclonic (low-pressure)
265 anomaly. At 400 hPa, significant westerly anomalies prevail in its southern flank, inducing the acceleration of westerlies
266 upstream of EAMBZ (**Fig. 3a**). At 850 hPa, the enhanced EAMBZ precipitation is connected to a north-south meridional
267 seesaw pattern, with a significant anticyclonic (high-pressure) anomaly over the subtropical western Pacific (SWP) and a
268 significant cyclonic anomaly over EAMBZ (**Fig. 3b**), exhibiting a somewhat barotropic structure (**Figs. 3a and 3b**).
269 Significant southerly anomalies prevail in the western flank of this SWP clockwise gyre anomaly (SWPCGA). Moreover,
270 from the perspective of $\langle \text{WVT} \rangle$ (**Fig. 3c**), the magnitudes of southerly $\langle \text{WVT} \rangle$ anomalies over the key EASM-controlled
271 domain tied to the SWPCGA are much greater than the westerly $\langle \text{WVT} \rangle$ anomalies over the westerly-dominated domain.
272 Note that the southerly $\langle \text{WVT} \rangle$ anomalies are significantly divergent, pushing copious amounts of warm and moist vapor
273 over the SWP into EAMBZ. Then, with the aid of the local anticlockwise $\langle \text{WVT} \rangle$ gyre pattern (**Fig. 3c**), the EASM
274 southerlies from the low latitudes, which bring warm temperature advection anomalies, may easily collide with the mid-
275 level cold temperature advection anomalies brought by mid-latitude enhanced westerlies (**Figs. 4a and 4b**), manifesting
276 the extratropical–tropical interplay around EAMBZ on interdecadal timescales. Such interplay is basically aligned with
277 that on interannual timescales (cf. Chen et al., 2021). Under such environments, atmospheric instability over EAMBZ can
278 be triggered to generate in situ significant ascending motion anomalies responsible for increased precipitation (**Fig. 5a**).
279 Note that considering the greater magnitudes of anomalies of $\langle \text{WVT} \rangle$ and warm temperature advection connected to the
280 southerlies over the key EASM-controlled domain, we presume that the monsoonal southerlies play a predominant
281 dynamical role in the interdecadal enhancement of precipitation over EAMBZ. To verify this presumption, we further
282 propose an East Asian monsoon index (I_{MI}), defined as the areal mean V850 over the key monsoonal southerly domain,
283 and a westerly index (I_{WI}), defined as the areal mean U400 over the upstream westerly-dominated region. The I_{MI} -
284 regressed results can well and realistically reproduce the magnitudes and distributions of the anomalous upward motions
285 tied to I_{EAMBZP} (**Fig. 5b** vs. **5a**). However, the magnitudes of I_{WI} -regressed results are highly weakened, along with the
286 major loadings shifting more southward (**Fig. 5c**). Above results could allow us to conclude that the anomalous southerlies
287 over the key monsoonal southerly domain could be the predominant driving factor for the interdecadal enhancement of
288 summer EAMBZ precipitation, whereas the upstream accelerated westerlies play a secondary dynamical amplification
289 role.

290

291 **3.2 Interdecadal relationship between IOBM and the summer EAMBZ precipitation**

292

293 Many previous studies have substantiated that the IOBM can remotely modulate summer rainfall fluctuations over the
294 mid-latitude Asia at interdecadal timescales (e.g., Zhang et al., 2018; S. Wang et al., 2022; Wu et al., 2022). In the present
295 study, we also identify that the IOBM can exert profound impacts on the interdecadal variations of the EAMBZ
296 precipitation in boreal summer. In this subsection, we firstly reveal their intimate relationship. **Figure 6a** exhibits the



297 correlation pattern between the JJA-mean I_{EAMBZP} and the contemporaneous global gridded SST at interdecadal timescales.
298 The most pronounced and significant correlations are found in the TIO sector, which largely matches the domain for
299 delineating the IOBM mode (black frame in **Fig. 6a**). There exists a salient out-of-phase relationship between the
300 interdecadal EAMBZ precipitation changes and the IOBM mode, with a TCC of -0.57 between I_{EAMBZP} and I_{IOBM} (**Fig.**
301 **6b**; $P < 0.01$). This result suggests that IOBM warming (cooling) is significantly connected with dry (wet) EAMBZ
302 summers, which serves as a critical oceanic modulator. On interdecadal timescales, the IOBM can remotely spark
303 conducive dynamical circumstances for increased precipitation over EAMBZ, i.e., the collision between cold and warm
304 airflows around EAMBZ (**Figs. 4c** and **4d**) and the locally significant convergent ascending motion anomalies resembled
305 those tied to the positive I_{EAMBZP} (**Fig. 5d** vs. **5a**). However, the extratropical cold (tropical warm) temperature advection
306 anomalies west (south) of the EAMBZ, which are tied to the strengthened westerlies (southerlies), are quite insignificant
307 (significant) (**Figs. 4c** and **4d**). This indicates that the IOBM may exert a more profound influence on the southerly wind
308 anomalies over the EASM-controlled domain, which is more important for enhanced EAMBZ precipitation; whereas the
309 IOBM may insignificantly modulate the westerly anomalies over the westerly-dominated region. The possible underlying
310 mechanisms of how IOBM links the summertime circulation anomalies responsible for the interdecadal fluctuations in
311 the EAMBZ precipitation will be illuminated in the next subsection.

312

313 3.3 Possible mechanisms

314

315 **Figure 7** shows partial regression of the JJA-mean anomalies of SST and large-scale precipitation over TIO and its
316 neighboring areas onto the I_{IOBM} at interdecadal timescales with the IPO signal removed. Corresponding to higher I_{IOBM}
317 years, warm SSTAs cover almost all areas of TIO, with large loadings appearing in the central-southern TIO and relatively
318 small loadings appearing in the northern TIO (**Fig. 7a**), which are aligned with the previous studies (Wu et al., 2016; Y.
319 Huang et al., 2019). Moreover, there are striking suppressed precipitation around the northeast corner of the TIO domain
320 (**Fig. 7b**), suggesting profoundly localized atmospheric responses to the warm TIO SSTAs. Note that there exist positive
321 precipitation anomalies around the northeast corner of TIO during the cold TIO SST years, suggesting the release of
322 anomalous atmospheric heating. Since the significant out-of-phase relationship between summertime IOBM and EAMBZ
323 precipitation at interdecadal timescales, we adopt negative I_{IOBM} -regressed patterns to express the influence of cold SSTAs
324 over the TIO region. **Figure 8** displays the anomalous patterns of the RWS, velocity potential, and divergent horizontal
325 winds regressed onto the negative I_{IOBM} . The velocity potential anomalies with larger negative (positive) loadings in the
326 upper (lower) troposphere are concentrated surrounding the northeast corner of TIO. Under these circumstances, local
327 upper (lower) tropospheric divergence (convergence) and negative (positive) RWS anomalies can be observed (**Fig. 8**),
328 suggesting enhanced ascending motions and convection activities in situ and thereby exciting the localized increased
329 precipitation/atmospheric heating. The above results indicate that IOBM cooling may transmit its interdecadal influence
330 via the intermediate atmospheric bridge of enhanced convective activities around the northeast corner of TIO, exerting a
331 remote modulation on the interdecadal EAMBZ rainfall variations.

332

333 Next, we further discuss the physical pathway linking IOBM cooling with the far-reaching downstream circulation
334 anomalies responsible for the interdecadal enhancement of EAMBZ precipitation, as shown in **Fig. 9**. Because the
335 cyclonic anomaly at 400 hPa shifts more eastward compared to the I_{EAMBZP} -regressed counterpart (**Fig. 9a** vs. **3a**), only
336 fractional westerly anomalies occupy the eastern part of the westerly-dominated region. The TCC between I_{IOBM} and I_{WI}
337 is nearly equal to zero ($r = -0.06$), thus linking the insignificant cold temperature advection displayed in **Fig. 4c**.
338 Nevertheless, in the lower troposphere, a “north-low–south-high” meridional seesaw pattern over the Northeast China–
339 SWP sector is found to be linked with IOBM cooling (**Fig. 9b**). Note that this negative I_{IOBM} -regressed seesaw pattern



340 exhibits a quasi-barotropic structure, with an anticlockwise <WVT> gyre in the north and a SWPCGA in the south (**Fig.**
341 **9c**), which is highly similar to that shown in **Fig. 3**. Significant anomalies of V850 and southerly <WVT> prevail over
342 the key monsoonal southerly domain, lying on the western flank of SWPCGA (**Figs. 9b** and **c**). The TCC between I_{IOBM}
343 and I_{MI} is -0.33 , significant at 0.05 on interdecadal timescales, thereby linking the significant warm temperature advection
344 anomalies indicated in **Fig. 4d**.

345

346 One may ask how IOBM cooling induces the above-mentioned meridional seesaw pattern. Previously, we have revealed
347 that negative SSTAs over TIO may exert remote interdecadal impacts through an atmospheric bridge, i.e., vigorous
348 convective activities around the northeast corner of TIO (**Figs. 7** and **8**). In effect, there exists a low-level cyclonic
349 anomaly in situ (**Fig. 9b**). Such cyclonic anomaly can be interpreted as a typical Gill–Matsuno-type response to regional
350 atmospheric heating caused by IOBM cooling (Matsuno, 1966; Gill, 1980), which is more clear within the lower levels
351 (**Fig. 9b**). As a result, consistent easterly anomalies appear from SWP to its northern flank around 15°N , denoting the
352 active role of depressed air pressure. The consistent easterly anomalies over SWP could lead to local anticyclonic wind
353 shear anomalies (Wang et al., 2019). In such a scenario, a quasi-barotropic SWPCGA can be induced (**Fig. 9**). Further,
354 local downward motions tied to SWPCGA could induce significant upward motions to its north via a meridional
355 overturning circulation (J. Wang et al., 2021), thus exciting a quasi-barotropic cyclonic anomaly and an anticlockwise
356 <WVT> gyre pattern centered over Northeast China (**Fig. 9**). Therefore, positive summertime rainfall anomalies over
357 EAMBZ at interdecadal timescales can be induced.

358

359 **3.4 Estimation of the interdecadal variations of summer EAMBZ precipitation**

360

361 In the last two subsections, we suggest that the IOBM cooling can serve as a significant oceanic modulator for increased
362 summer EAMBZ precipitation at interdecadal timescales, and present the corresponding physical mechanisms. To
363 estimate their steady antiphase relationship, in the following, the negative I_{IOBM} is selected to construct a physical-based
364 empirical (P-E) model by using the simple linear regression (SLR) analysis and the cross-validation method (You and Jia,
365 2018; Chang et al., 2021; Jeong et al., 2021), representing the impact of IOBM cooling. The P-E model is given as follows:

366

$$367 I_{EAMBZP} = \beta_0 + \beta_1 I_{IOBM} + \varepsilon, \quad (5)$$

368

369 where β_0 and β_1 are regression coefficients, and ε denotes the residuals. The time series of I_{EAMBZP} and I_{IOBM} are detrended
370 and 11-year low-pass filtered beforehand.

371

372 Following Jeong et al. (2021), a “leaving one out” cross-validation strategy is employed to determine the robustness of
373 the hindcast estimates. The normalized time series of summer I_{EAMBZP} and associated leave-one-out cross-validated
374 hindcast estimates are shown in **Fig. 10**. The TCC between P-E predicted hindcast estimates (blue line) and the observed
375 I_{EAMBZP} (red line) for 1901–2014 can reach 0.56 ($P < 0.05$), suggesting that the P-E model can well capture the interdecadal
376 I_{EAMBZP} variations and reflect their steady relationship.

377

378 **4 Discussion**

379

380 Numerous recent studies employed the pacemaker experiments that restore the historical observational basin-wide SSTAs
381 to validate the mechanisms of how remote SSTAs over the Pacific Ocean, the Atlantic Ocean, and the Indian Ocean
382 modulate the climate anomalies in many areas across the globe at interdecadal timescale (e.g., Yang et al., 2020; Jiang et



383 [al., 2021; J. Wang et al., 2022](#)). As proposed in Section 2.6, there exists a considerably high positive TCC between the
384 broader TIO SSTAs regarding CESM1_IOPES and narrower TIO SSTAs regarding IOBM in both observations and
385 simulations. Furthermore, the simulated large and strong loadings of SSTAs concentrate over the central-southern TIO
386 (**Fig. S4b**), delineating a quite similar distribution with that in the observation (**Figs. 7a** and **S4a**). As a consequence, we
387 use the pacemaker experimental data based on the ensemble mean of CESM1_IOPES and CESM1_LENS to validate our
388 proposed mechanisms regarding the modulation of IOBM cooling on the interdecadal enhancement of summer EAMBZ
389 precipitation. Considering the predominant role of southerly anomalies over the key monsoonal southerly domain, we
390 therefore emphasize the low-level (850 hPa) atmospheric anomalies at interdecadal timescales tied to the IOBM-like SST
391 cooling, as depicted in **Fig. 11**. We can observe a clearly anomalous cyclonic circulation around the northeast corner of
392 TIO, accompanied by local positive precipitation anomalies and easterly anomalies that stretch from SWP to its northern
393 flank, which are generally resembled those in the observation (**Figs. 7b** and **9b**). In this circumstance, a similar “north-
394 low–south-high” meridional seesaw pattern over the Northeast China–SWP sector can be formed to spark and sustain the
395 enhanced EAMBZ precipitation in boreal summer (**Fig. 11**). However, although the results from CESM1_LENS and
396 CESM1_IOPES can reasonably confirm our proposed physical pathway of how IOBM cooling exerts a distant modulation
397 on the interdecadal enhancement of summer precipitation over EAMBZ, we can still notice the weakness of the model
398 simulations. That is, positive precipitation anomalies around the northeast corner of TIO and the easterly anomalies
399 exhibit weaker magnitudes compared to the observations (**Fig. 11** vs. **7b** and **9b**). Besides, systematic biases exist
400 regarding the simulated positions of the upper (lower) tropospheric divergence (convergence) and negative (positive)
401 RWS anomalies (**Fig. S5**), manifesting themselves in the eastward displacement tendency in contrast to those around the
402 northeast corner of the TIO (**Fig. 8**).

403
404

5 Conclusions

405

406 In this study, by analysis of the long-term observational and reanalysis datasets during 1901–2014, the temporal
407 characteristics of interdecadal variations in the summer EAMBZ precipitation and associated circulation background are
408 revealed. The potential modulation of IOBM on the variations is further discussed.

409

410 The summer EAMBZ precipitation exhibited a salient interdecadal fluctuations, e.g., with dry summers during the periods
411 preceding 1927, 1968–1982, and 1998–2010, as well as wet summers during the periods of 1928–1938, 1946–1967, and
412 2011 onwards. It is indicated that the cold airflows brought by the mid-latitude accelerated upstream westerlies over the
413 westerly-dominated domain collide and converge with the warm and humid airflows brought by the enhanced southerlies
414 over the key EASM-controlled domain, suggesting the local extratropical–tropical interplay. Further diagnostic results
415 suggest that the monsoonal southerly anomalies could be viewed as the predominant driving factor for the interdecadal
416 enhancement of EAMBZ precipitation, whereas the upstream westerlies play a secondary dynamical amplification role.
417 Such circulation anomalies are closely linked to a “north-low–south-high” meridional seesaw pattern over the Northeast
418 China–SWP sector, which provides favorable environments for the transportation of water vapor from the SWP and the
419 convergence over EAMBZ to spark enhanced summer EAMBZ precipitation at interdecadal timescales.

420

421 We further identify that the IOBM-related SST anomaly pattern is a salient oceanic modulator for the interdecadal
422 variations of the summer EAMBZ precipitation via the Gill–Matsumoto mechanism. When the cold phase of the IOBM
423 occurs, an anomalous cyclonic circulation is excited around the northeast corner of TIO. As a response, consistent easterly
424 anomalies appear from SWP to its northern flank, leading to local anticyclonic wind shear anomalies and thus inducing a
425 SWPCGA pattern and a resultant anticlockwise gyre pattern centered over Northeast China. On interdecadal timescales,



426 such meridional seesaw pattern tied to the IOBM cooling is responsible for enhanced summer precipitation over EAMBZ
427 through linking the predominant driving factor of strengthened monsoonal southerly anomalies west of the SWPCGA
428 pattern. As such, the water vapor transportation from the SWP and the convergence over EAMBZ can be triggered to
429 induce and sustain the enhancement local precipitation. Correspondingly, a P-E model based the negative I_{IOBM} is
430 constructed, which can well capture the interdecadal fluctuations in the EAMBZ precipitation and reflect their steady
431 relationship. Furthermore, the results based on the large ensemble experiment and the Indian Ocean pacemaker
432 experiment also confirm the crucial physical pathway linking the SST variations over TIO with the summer precipitation
433 over EAMBZ via the influence of SST variations on the aforementioned meridional seesaw pattern at interdecadal
434 timescales.

435
436

437 **Code and data availability.** The CRU TS precipitation data version 3.26 (CRU TS3.26) from CRU at the University of
438 East Anglia are available online (<https://catalogue.ceda.ac.uk/uuid/3f894480cc48e1cbc29a5ee12d8542d>; [CRU, 2022](#)).
439 The ERSSTv5 data from the US NOAA are available from the following website:
440 <https://www1.ncdc.noaa.gov/pub/data/cmb/ersst/v5/netcdf/> ([NOAA 2020](#)). The 20CRv2c datasets from NOAA-CIRES
441 are available from the following website: https://psl.noaa.gov/data/gridded/data.20thC_ReanV2c.html ([NOAA-CIRES,](#)
442 [2022](#)). The model simulation datasets regarding CESM1_LENS are available online
443 (<https://www.cesm.ucar.edu/community-projects/lens/data-sets/>; [NCAR 2023](#)). The model simulation datasets regarding
444 CESM1_IOPES are available online (<https://www.earthsystemgrid.org/dataset/ucar.cgd.cesm4.IOD-PACEMAKER.html>;
445 [NCAR 2023](#)).

446 Codes are available from the corresponding author on reasonable request.

447

448 **Author contributions.** YL designed the research; JW wrote the first draft of the paper; FC and CS downloaded and
449 analyzed the data, and plotted the figures used in this study. All authors, including YD and XX, contributed to the
450 discussion of the results and reviewed the manuscript.

451

452 **Competing Interests.** The contact author has declared that none of the authors has any competing interests.

453

454 **Acknowledgements.** Yanju Liu acknowledges the support by the Key Innovation Team of China Meteorological
455 Administration “Climate Change Detection and Response” (CMA2022ZD03).

456 **Financial support.** This study was supported by the Second Tibetan Plateau Scientific Expedition and Research (STEP)
457 program (2019QZKK010204-02 and 2019QZKK0102), Guangdong Major Project of Basic and Applied Basic Research
458 (2020B0301030004), and Innovation and Development Special Project of China Meteorological Administration
459 (CXFZ2022J039).

460

461

462 References

463

464 Chang, L., Wu, Z. and Xu, J., 2021. Contribution of Northeastern Asian stratospheric warming to subseasonal prediction
465 of the early winter haze pollution in Sichuan Basin, China. *Science of the Total Environment*, 751: 141823.

466 Chen, F.-H., Chen, J.-H., Holmes, J., Boomer, I., Austin, P., Gates, J.B., Wang, N.-L., Brooks, S.J. and Zhang, J.-W., 2010.
467 Moisture changes over the last millennium in arid central Asia: a review, synthesis and comparison with monsoon
468 region. *Quaternary Science Reviews*, 29(7): 1055-1068.

469 Chen, J., Huang, W., Feng, S., Zhang, Q., Kuang, X., Chen, J. and Chen, F., 2021. The modulation of westerlies-monsoon
470 interaction on climate over the monsoon boundary zone in East Asia. *International Journal of Climatology*,



- 471 41(S1): E3049-E3064.
- 472 Chen, J., Huang, W., Jin, L., Chen, J., Chen, S. and Chen, F., 2018. A climatological northern boundary index for the East
473 Asian summer monsoon and its interannual variability. *Science China Earth Sciences*, 61(1): 13-22.
- 474 Compo, G.P., Whitaker, J.S., Sardeshmukh, P.D., Matsui, N., Allan, R.J., Yin, X., Gleason, B.E., Vose, R.S., Rutledge, G.,
475 Bessemoulin, P., Brönnimann, S., Brunet, M., Crouthamel, R.I., Grant, A.N., Groisman, P.Y., Jones, P.D., Kruk,
476 M.C., Kruger, A.C., Marshall, G.J., Maugeri, M., Mok, H.Y., Nordli, Ø., Ross, T.F., Trigo, R.M., Wang, X.L.,
477 Woodruff, S.D. and Worley, S.J., 2011. The Twentieth Century Reanalysis Project. *Quarterly Journal of the Royal
478 Meteorological Society*, 137(654): 1-28.
- 479 CRU: CRU TS3.26, monthly, CRU [data set] <https://catalogue.ceda.ac.uk/uuid/3f894480cc48e1cbc29a5ee12d8542d>,
480 last access: 5 July 2022.
- 481 Ding, Y. and Chan, J.C.L., 2005. The East Asian summer monsoon: an overview. *Meteorology and Atmospheric Physics*,
482 89(1): 117-142.
- 483 Dou, J. and Wu, Z., 2018. Southern Hemisphere origins for interannual variations of snow cover over the western Tibetan
484 Plateau in boreal summer. *Journal of Climate*, 31(19): 7701-7718.
- 485 Duchon, C.E., 1979. Lanczos filtering in one and two dimensions. *Journal of Applied Meteorology and Climatology*,
486 18(8): 1016-1022.
- 487 Gill, A.E., 1980. Some simple solutions for heat-induced tropical circulation. *Quarterly Journal of the Royal
488 Meteorological Society*, 106(449): 447-462.
- 489 Han, W., Vialard, J., McPhaden, M.J., Lee, T., Masumoto, Y., Feng, M. and de Ruijter, W.P.M., 2014. Indian Ocean
490 decadal variability: A review. *Bulletin of the American Meteorological Society*, 95(11): 1679-1703.
- 491 Harris, I., Jones, P.D., Osborn, T.J. and Lister, D.H., 2014. Updated high-resolution grids of monthly climatic
492 observations—the CRU TS3.10 Dataset. *International Journal of Climatology*, 34(3): 623-642.
- 493 Henley, B.J., Gergis, J., Karoly, D.J., Power, S., Kennedy, J. and Folland, C.K., 2015. A Tripole Index for the Interdecadal
494 Pacific Oscillation. *Climate Dynamics*, 45(11): 3077-3090.
- 495 Huang, B., Thorne, P.W., Banzon, V.F., Boyer, T., Chepurin, G., Lawrimore, J.H., Menne, M.J., Smith, T.M., Vose, R.S.
496 and Zhang, H.-M., 2017. Extended Reconstructed Sea Surface Temperature, version 5 (ERSSTv5): Upgrades,
497 validations, and intercomparisons. *Journal of Climate*, 30(20): 8179-8205.
- 498 Huang, J., Li, Y., Fu, C., Chen, F., Fu, Q., Dai, A., Shinoda, M., Ma, Z., Guo, W., Li, Z., Zhang, L., Liu, Y., Yu, H., He,
499 Y., Xie, Y., Guan, X., Ji, M., Lin, L., Wang, S., Yan, H. and Wang, G., 2017. Dryland climate change: Recent
500 progress and challenges. *Reviews of Geophysics*, 55(3): 719-778.
- 501 Huang, J., Ma, J., Guan, X., Li, Y. and He, Y., 2019. Progress in semi-arid climate change studies in China. *Advances in
502 Atmospheric Sciences*, 36(9): 922-937.
- 503 Huang, J., Zhang, G., Zhang, Y., Guan, X., Wei, Y. and Guo, R., 2020. Global desertification vulnerability to climate
504 change and human activities. *Land Degradation & Development*, 31(11): 1380-1391.
- 505 Huang, W., Chen, J., Zhang, X., Feng, S. and Chen, F., 2015. Definition of the core zone of the “westerlies-dominated
506 climatic regime”, and its controlling factors during the instrumental period. *Science China Earth Sciences*, 58(5):
507 676-684.
- 508 Huang, Y., Wu, B., Li, T., Zhou, T. and Liu, B., 2019. Interdecadal Indian Ocean basin mode driven by interdecadal
509 Pacific oscillation: A season-dependent growth mechanism. *Journal of Climate*, 32(7): 2057-2073.
- 510 Hurrell, J.W., Holland, M.M., Gent, P.R., Ghan, S., Kay, J.E., Kushner, P.J., Lamarque, J.F., Large, W.G., Lawrence, D.,
511 Lindsay, K., Lipscomb, W.H., Long, M.C., Mahowald, N., Marsh, D.R., Neale, R.B., Rasch, P., Vavrus, S.,
512 Vertenstein, M., Bader, D., Collins, W.D., Hack, J.J., Kiehl, J. and Marshall, S., 2013. The Community Earth
513 System Model: A framework for collaborative research. *Bulletin of the American Meteorological Society*, 94(9):
514 1339-1360.
- 515 Jeong, J.I., Park, R.J., Yeh, S.-W. and Roh, J.-W., 2021. Statistical predictability of wintertime PM_{2.5} concentrations over
516 East Asia using simple linear regression. *Science of the Total Environment*, 776: 146059.
- 517 Jiang, J., Zhou, T., Chen, X. and Wu, B., 2021. Central Asian precipitation shaped by the tropical Pacific decadal
518 variability and the Atlantic multidecadal variability. *Journal of Climate*, 34(18): 7541-7553.
- 519 Kay, J.E., Deser, C., Phillips, A., Mai, A., Hannay, C., Strand, G., Arblaster, J.M., Bates, S.C., Danabasoglu, G., Edwards,



- 520 J., Holland, M., Kushner, P., Lamarque, J.F., Lawrence, D., Lindsay, K., Middleton, A., Munoz, E., Neale, R.,
521 Oleson, K., Polvani, L. and Vertenstein, M., 2015. The community earth system model (CESM) large ensemble
522 project: a community resource for studying climate change in the presence of internal climate variability. *Bulletin*
523 *of the American Meteorological Society*, 96(8): 1333-1349.
- 524 Klein, S.A., Soden, B.J. and Lau, N.-C., 1999. Remote sea surface temperature variations during ENSO: evidence for a
525 tropical atmospheric bridge. *Journal of Climate*, 12(4): 917-932.
- 526 Li, J., Sun, C. and Jin, F.-F., 2013. NAO implicated as a predictor of Northern Hemisphere mean temperature multidecadal
527 variability. *Geophysical Research Letters*, 40(20): 5497-5502.
- 528 Li, J. and Zeng, Q., 2002. A unified monsoon index. *Geophysical Research Letters*, 29(8): 115-1-115-4.
- 529 Li, M. and Ma, Z., 2018. Decadal changes in summer precipitation over arid northwest China and associated atmospheric
530 circulations. *International Journal of Climatology*, 38(12): 4496-4508.
- 531 Lu, W. and Jia, G., 2013. Fluctuation of farming-pastoral ecotone in association with changing East Asia monsoon climate.
532 *Climatic Change*, 119(3): 747-760.
- 533 Mastyo, M., 2013. Bilinear interpolation theorems and applications. *Journal of Functional Analysis*, 265(2): 185-207.
- 534 Matsuno, T., 1966. Quasi-geostrophic motions in the equatorial area. *Journal of the Meteorological Society of Japan*,
535 44(1): 25-43.
- 536 Moss, R.H., Edmonds, J.A., Hibbard, K.A., Manning, M.R., Rose, S.K., van Vuuren, D.P., Carter, T.R., Emori, S.,
537 Kainuma, M., Kram, T., Meehl, G.A., Mitchell, J.F.B., Nakicenovic, N., Riahi, K., Smith, S.J., Stouffer, R.J.,
538 Thomson, A.M., Weyant, J.P. and Wilbanks, T.J., 2010. The next generation of scenarios for climate change
539 research and assessment. *Nature*, 463(7282): 747-756.
- 540 NCAR: CESM1_LENS, monthly, NCAR [data set] <https://www.cesm.ucar.edu/community-projects/lens/data-sets>, last
541 access: 28 April 2023.
- 542 NCAR: CESM1_IOPES, monthly, NCAR [data set] [https://www.earthsystemgrid.org/dataset/ucar.cgd.cesm4.IOD-](https://www.earthsystemgrid.org/dataset/ucar.cgd.cesm4.IOD-PACEMAKER.html)
543 [PACEMAKER.html](https://www.earthsystemgrid.org/dataset/ucar.cgd.cesm4.IOD-PACEMAKER.html), last access: 4 May 2023.
- 544 NOAA: ERSSTv5, monthly, NOAA [data set] <https://www1.ncdc.noaa.gov/pub/data/cmb/ersst/v5/netcdf/>, last access: 15
545 October 2020.
- 546 NOAA-CIRES: 20CRv2c, monthly, NOAA-CIRES [data set]
547 https://psl.noaa.gov/data/gridded/data.20thC_ReanV2c.html, last access: 26 June 2022.
- 548 North, G.R., Bell, T.L., Cahalan, R.F. and Moeng, F.J., 1982. Sampling errors in the estimation of empirical orthogonal
549 functions. *Monthly Weather Review*, 110(7): 699-706.
- 550 Ou, T.H. and Qian, W.H., 2006. Vegetation variations along the monsoon boundary zone in East Asia. *Chinese Journal of*
551 *Geophysics (in Chinese)*, 49(3): 698-705.
- 552 Piao, J., Chen, W. and Chen, S., 2021. Water vapour transport changes associated with the interdecadal decrease in the
553 summer rainfall over Northeast Asia around the late-1990s. *International Journal of Climatology*, 41(S1): E1469-
554 E1482.
- 555 Qian, W., Ding, T., Hu, H., Lin, X. and Qin, A., 2009. An overview of dry-wet climate variability among monsoon-
556 westerly regions and the monsoon northernmost marginal active zone in China. *Advances in Atmospheric*
557 *Sciences*, 26(4): 630-641.
- 558 Sardeshmukh, P.D. and Hoskins, B.J., 1988. The generation of global rotational flow by steady idealized tropical
559 divergence. *Journal of Atmospheric Sciences*, 45(7): 1228-1251.
- 560 Schiemann, R., Lüthi, D. and Schär, C., 2009. Seasonality and interannual variability of the westerly jet in the Tibetan
561 Plateau region. *Journal of Climate*, 22(11): 2940-2957.
- 562 Si, D. and Ding, Y., 2016. Oceanic forcings of the interdecadal variability in East Asian summer rainfall. *Journal of*
563 *Climate*, 29(21): 7633-7649.
- 564 Si, D., Jiang, D., Hu, A. and Lang, X., 2021. Variations in northeast Asian summer precipitation driven by the Atlantic
565 multidecadal oscillation. *International Journal of Climatology*, 41(3): 1682-1695.
- 566 Song, C., Wang, J., Liu, Y., Zhang, L., Ding, Y., Li, Q., Shen, X., Song, Y. and Yan, Y., 2022. Toward role of westerly-
567 monsoon interplay in linking interannual variations of late spring precipitation over the southeastern Tibetan
568 Plateau. *Atmospheric Science Letters*, 23(3): e1074.



- 569 Sun, B., Li, H. and Zhou, B., 2019a. Interdecadal variation of Indian Ocean basin mode and the impact on Asian summer
570 climate. *Geophysical Research Letters*, 46(21): 12388-12397.
- 571 Sun, B., Wang, H., Zhou, B. and Li, H., 2019b. Interdecadal variation in the synoptic features of mei-yu in the Yangtze
572 River valley region and relationship with the Pacific decadal oscillation. *Journal of Climate*, 32(19): 6251-6270.
- 573 Taylor, K.E., Stouffer, R.J. and Meehl, G.A., 2012. An overview of CMIP5 and the experiment design. *Bulletin of the*
574 *American Meteorological Society*, 93(4): 485-498.
- 575 Touma, D., Stevenson, S., Lehner, F. and Coats, S., 2021. Human-driven greenhouse gas and aerosol emissions cause
576 distinct regional impacts on extreme fire weather. *Nature Communications*, 12(1): 212.
- 577 Wang, B., Wu, Z., Li, J., Liu, J., Chang, C.-P., Ding, Y. and Wu, G., 2008. How to measure the strength of the East Asian
578 summer monsoon. *Journal of Climate*, 21(17): 4449-4463.
- 579 Wang, J., Zhu, Z.W., Qi, L., Zhao, Q.H., He, J.H. and Wang, J.X.L., 2019. Two pathways of how remote SST anomalies
580 drive the interannual variability of autumnal haze days in the Beijing–Tianjin–Hebei region, China. *Atmospheric*
581 *Chemistry and Physics*, 19(3): 1521-1535.
- 582 Wang, J., Liu, Y., Ding, Y. and Wu, Z., 2021. Towards influence of Arabian Sea SST anomalies on the withdrawal date of
583 Meiyu over the Yangtze-Huaihe River basin. *Atmospheric Research*, 249: 105340.
- 584 Wang, J., Liu, Y., Song, C., Ding, Y., Li, Q., Wu, P., Xu, Y. and Xu, X., 2022. Synergistic impacts of westerlies and
585 monsoon on interdecadal variations of late spring precipitation over the southeastern extension of the Tibetan
586 Plateau. *International Journal of Climatology*, 42(14): 7342-7361.
- 587 Wang, J., Liu, Y., Yang, Y., Wu, P., Yang, J., Liang, P., Song, C., Zhang, S. and Ding, Y., 2023. Impact of early winter
588 North Atlantic Oscillation on the dramatic alternation of seesaw haze intensity between late winter months in
589 the North China Plain. *Atmospheric Research*, 281: 106483.
- 590 Wang, L., Chen, W., Huang, G. and Zeng, G., 2017. Changes of the transitional climate zone in East Asia: past and future.
591 *Climate Dynamics*, 49(4): 1463-1477.
- 592 Wang, Q., Wang, L., Huang, G., Piao, J. and Chotamonsak, C., 2021. Temporal and spatial variation of the transitional
593 climate zone in summer during 1961–2018. *International Journal of Climatology*, 41(3): 1633-1648.
- 594 Wang, Q., Wang, L., Huang, G. and Wang, T., 2022. Mechanism of the summer rainfall interannual variability in
595 transitional climate zone in East Asia: roles of teleconnection patterns and associated moisture processes.
596 *Climate Dynamics*, <https://doi.org/10.1007/s00382-022-06618-1>.
- 597 Wang, Q., Huang, G., Wang, L., Piao, J., Ma, T., Hu, P., Chotamonsak, C. and Limsakul, A., 2023. Mechanism of the
598 summer rainfall variation in Transitional Climate Zone in East Asia from the perspective of moisture supply
599 during 1979–2010 based on the Lagrangian method. *Climate Dynamics*, 60(3): 1225-1238.
- 600 Wang, S., Huang, J., Huang, G., Luo, F., Ren, Y. and He, Y., 2022. Enhanced impacts of Indian Ocean sea surface
601 temperature on the dry/wet variations over Northwest China. *Journal of Geophysical Research: Atmospheres*,
602 127(11): e2022JD036533.
- 603 Wu, B., Zhou, T. and Li, T., 2016. Impacts of the Pacific–Japan and circumglobal teleconnection patterns on the
604 interdecadal variability of the East Asian summer monsoon. *Journal of Climate*, 29(9): 3253-3271.
- 605 Wu, G., Guan, Y., Liu, Y., Yan, J. and Mao, J., 2012. Air–sea interaction and formation of the Asian summer monsoon
606 onset vortex over the Bay of Bengal. *Climate Dynamics*, 38(1): 261-279.
- 607 Wu, P., Liu, Y., Ding, Y., Li, X. and Wang, J., 2022. Modulation of sea surface temperature over the North Atlantic and
608 Indian-Pacific warm pool on interdecadal change of summer precipitation over northwest China. *International*
609 *Journal of Climatology*, 42(16): 8526-8538.
- 610 Xie, S.-P., Hu, K., Hafner, J., Tokinaga, H., Du, Y., Huang, G. and Sampe, T., 2009. Indian Ocean capacitor effect on
611 Indo–western Pacific climate during the summer following El Niño. *Journal of Climate*, 22(3): 730-747.
- 612 Xing, W. and Wang, B., 2017. Predictability and prediction of summer rainfall in the arid and semi-arid regions of China.
613 *Climate Dynamics*, 49(1): 419-431.
- 614 Yang, D., Arblaster, J.M., Meehl, G.A., England, M.H., Lim, E.-P., Bates, S. and Rosenbloom, N., 2020. Role of tropical
615 variability in driving decadal shifts in the Southern Hemisphere summertime eddy-driven jet. *Journal of Climate*,
616 33(13): 5445-5463.
- 617 Yang, J., Liu, Q., Xie, S.-P., Liu, Z. and Wu, L., 2007. Impact of the Indian Ocean SST basin mode on the Asian summer



618 monsoon. *Geophysical Research Letters*, 34(2): L02708.

619 Yeh, T.-C., Dao, S.-Y. and Li, M.-T., 1959. The abrupt change of circulation over the Northern Hemisphere during June
620 and October. *The Atmosphere and the Sea in Motion*, the Rockefeller Institute Press and Oxford University Press,
621 249-267.

622 Ying, K., Jiang, D., Zheng, X., Frederiksen, C.S., Peng, J., Zhao, T. and Zhong, L., 2023. Seasonal predictable source of
623 the East Asian summer monsoon rainfall in addition to the ENSO–AO. *Climate Dynamics*, 60(7): 2459-2480.

624 You, Y. and Jia, X., 2018. Interannual variations and prediction of spring precipitation over China. *Journal of Climate*,
625 31(2): 655-670.

626 Zeng, J. and Zhang, Q., 2019. A humidity index for the summer monsoon transition zone in East Asia. *Climate Dynamics*,
627 53(9): 5511-5527.

628 Zhang, L., Han, W., Karauskas, K.B., Meehl, G.A., Hu, A., Rosenbloom, N. and Shinoda, T., 2019. Indian Ocean
629 warming trend reduces Pacific warming response to anthropogenic greenhouse gases: An interbasin thermostat
630 mechanism. *Geophysical Research Letters*, 46(19): 10882-10890.

631 Zhang, Z., Sun, X. and Yang, X.-Q., 2018. Understanding the interdecadal variability of East Asian summer monsoon
632 precipitation: Joint influence of three oceanic signals. *Journal of Climate*, 31(14): 5485-5506.

633 Zhao, W., Chen, S., Chen, W., Yao, S., Nath, D. and Yu, B., 2019a. Interannual variations of the rainy season withdrawal
634 of the monsoon transitional zone in China. *Climate Dynamics*, 53(3): 2031-2046.

635 Zhao, W., Chen, W., Chen, S., Yao, S.-L. and Nath, D., 2019b. Inter-annual variations of precipitation over the monsoon
636 transitional zone in China during August–September: Role of sea surface temperature anomalies over the
637 tropical Pacific and North Atlantic. *Atmospheric Science Letters*, 20(1): e872.

638 Zhao, W., Chen, W., Chen, S., Nath, D. and Wang, L., 2020. Interdecadal change in the impact of North Atlantic SST on
639 August rainfall over the monsoon transitional belt in China around the late 1990s. *Theoretical and Applied
640 Climatology*, 140(1): 503-516.

641

642

643

644

645

646

647

648

649

650

651

652

653

654

655

656

657

658

659

660

661

662

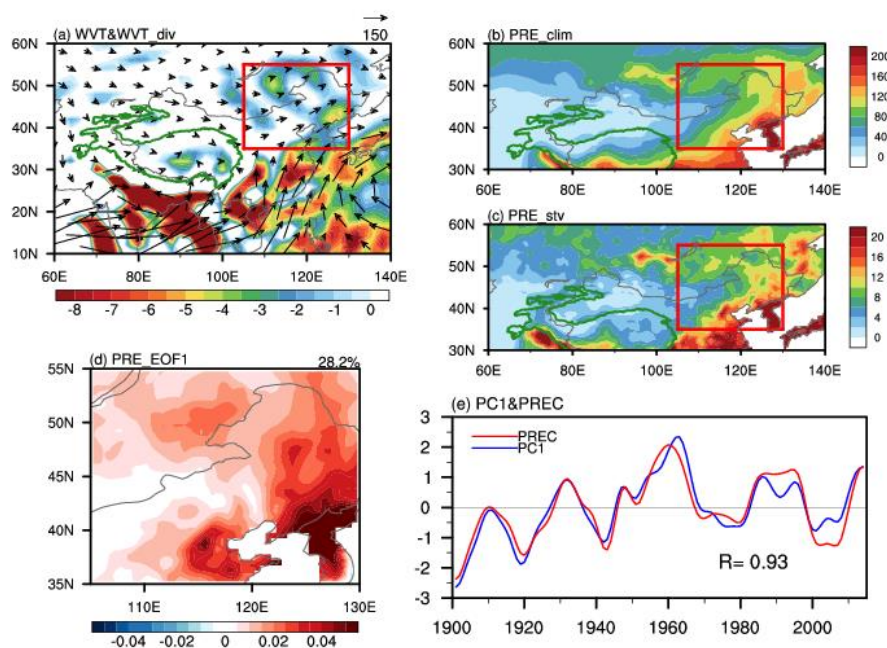
663

664



665 **Figures**

666



667

668

669

670

671

672

673

674

675

676

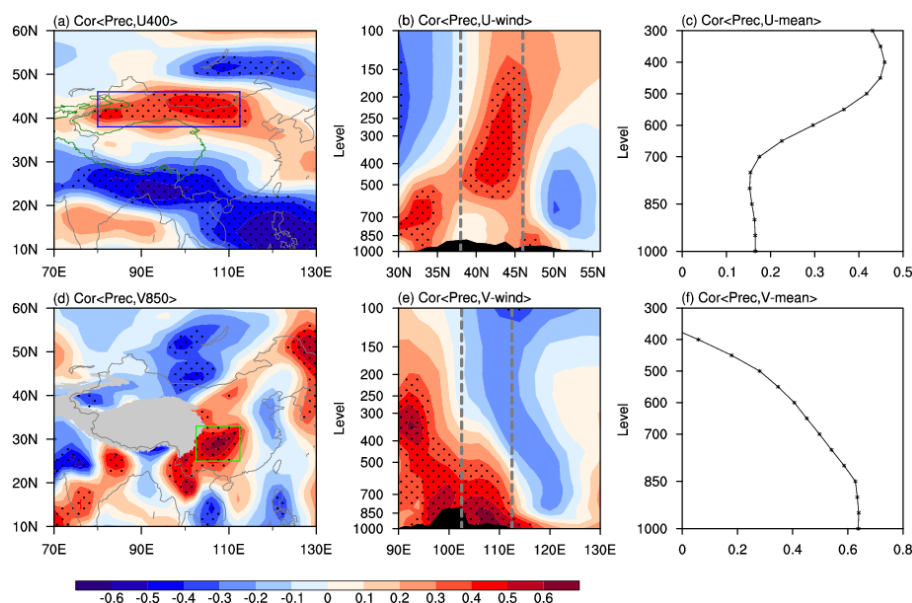
677

678

679

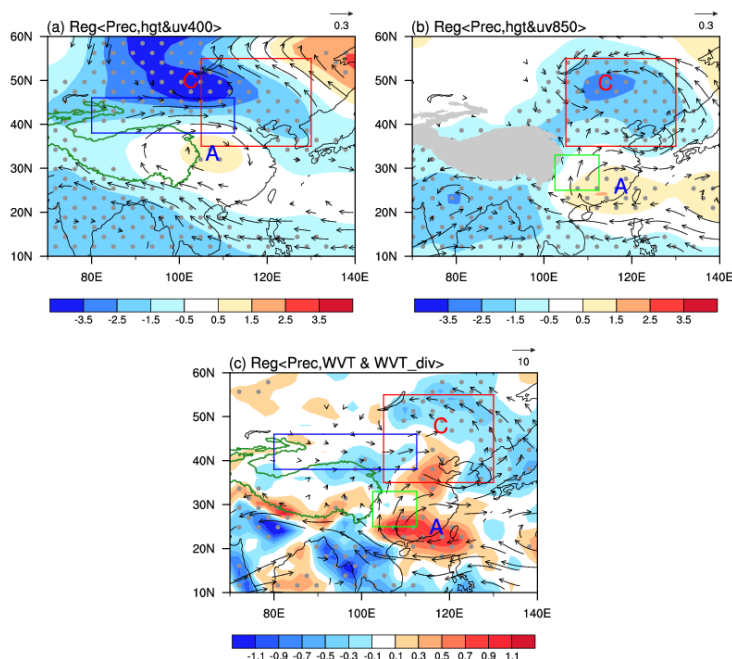
680

Figure 1. The climatological JJA-averaged (a) $\langle WVT \rangle$ (vectors; $\text{kg m}^{-1} \text{s}^{-1}$) and $\langle WVT_div \rangle$ (shading; $10^{-5} \text{ kg m}^{-2} \text{s}^{-1}$), (b) precipitation (mm month^{-1}), and (c) interdecadal standard deviation of precipitation (mm month^{-1}) during the period 1901–2014. The red box (35° – 55° N, 105° – 130° E) outlines the research domain of EAMBZ (the same hereinafter). (d) Spatial pattern of the first empirical orthogonal function (EOF1) mode of JJA-mean EAMBZ precipitation. (e) Normalized time series of the JJA-mean EAMBZ precipitation index (I_{EAMBZP}) (red line) and associated first principal component (PC1) (blue line), with the number denoting the temporal correlation coefficient (TCC) between the corresponding time series. In panels (c)–(e), variables are detrended and 11-year low-pass filtered. The green outline in panels (a)–(c) represents the terrain of the Tibetan Plateau (TP) at 2000 m (the same hereinafter). The precipitation is derived from the CRU TS3.26 precipitation data, while other variables are from the 20CRv2c datasets.



681
 682 **Figure 2.** Correlation maps of the JJA-averaged I_{EAMBZP} with the simultaneous (a) 400-hPa zonal wind (U400) and (d) 850-hPa
 683 meridional wind (V850), and (b) height–latitude cross-section of zonal winds averaged over 80° – 112.5° E, and (e) height–longitude
 684 cross-section of meridional winds averaged over 25° – 33° N, during the period 1901–2014. The blue box (38° – 46° N, 80° – 112.5° E) in
 685 (a) and the green box (25° – 33° N, 102.5° – 112.5° E) in (d) represent the upstream westerly domain and the monsoonal southerly domain
 686 significantly tied to the interdecadal variations of precipitation over EAMBZ, respectively (the same hereinafter). The grey-dashed
 687 vertical lines in (b) and (e) represent the latitudinal and longitudinal range of the westerly and the monsoonal southerly domain,
 688 respectively. (c) Profile of correlation coefficients between the JJA-averaged I_{EAMBZP} and the simultaneous area-averaged zonal winds
 689 over the upstream westerly domain at multiple levels during the period 1901–2014. (f) As in (c), but for the meridional winds over the
 690 monsoonal southerly domain. All variables are detrended and 11-year low-pass filtered. Areas with significant values exceeding the
 691 95% confidence level are stippled. The black shading indicates the topography. The grey shaded areas denote the TP areas above 2000
 692 m (the same hereinafter). The I_{EAMBZP} is calculated based on the CRU TS3.26 precipitation data, while other variables are from the
 693 20CRv2c datasets.

694
 695
 696
 697
 698
 699
 700
 701
 702
 703
 704



705

706 **Figure 3.** Regression maps of the JJA-mean anomalies of (a) 400-hPa geopotential height (Z400; shading; m) and wind field (UV400;
707 vectors; m s^{-1}), (b) 850-hPa geopotential height (Z850; shading; m) and wind field (UV850; vectors; m s^{-1}), and (c) $\langle \text{WVT} \rangle$ (vectors;
708 $\text{kg m}^{-1} \text{s}^{-1}$) and $\langle \text{WVT_div} \rangle$ (shading; $10^{-5} \text{ kg m}^{-2} \text{s}^{-1}$) onto the concurrent I_{EAMBZP} during the period 1901–2014. All variables are
709 detrended and 11-year low-pass filtered. Letter A (C) represents the center of anticyclonic (cyclonic) anomaly (the same hereinafter).
710 Areas with significant values of Z400, Z850, and $\langle \text{WVT_div} \rangle$ that exceed the 95% confidence level are stippled, respectively. Only
711 vectors that are significant at the 95% confidence level are shown. The I_{EAMBZP} is calculated based on the CRU TS3.26 precipitation
712 data, while other variables are from the 20CRv2c datasets.

713

714

715

716

717

718

719

720

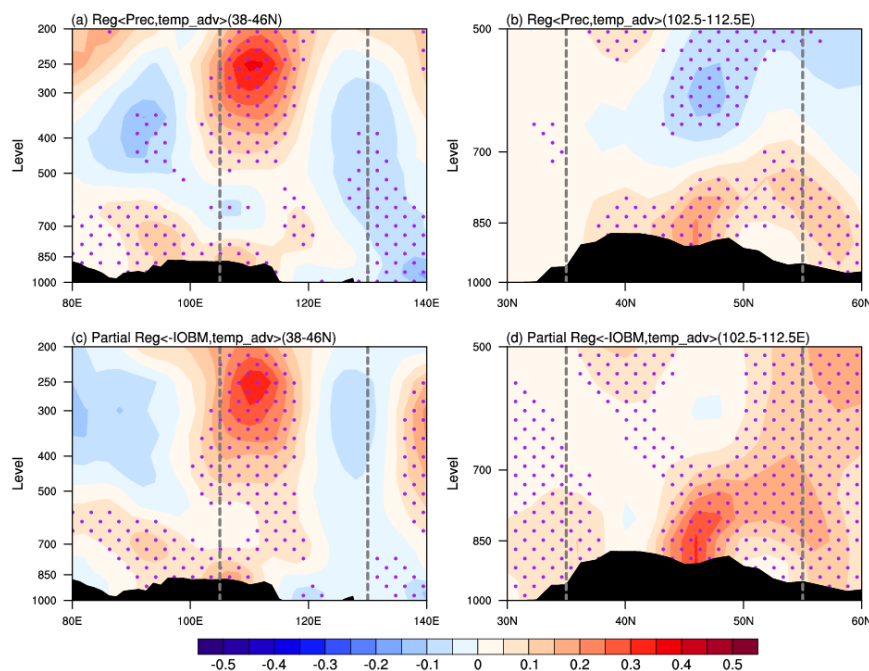
721

722

723

724

725



726

727 **Figure 4.** (a) Height–longitude cross-section (averaged over 38 °–46 °N) and (b) height–latitude cross-section (averaged over 102.5 °–
728 112.5 °E) of the JJA-mean temperature advection anomalies (shading; 10^{-5} K s^{-1}) regressed onto the concurrent I_{EAMBZ} during the
729 period 1901–2014. (c, d) As in (a, b), but for patterns of the partial regression coefficient between temperature advection and negative
730 I_{IOBM} without the IPO signal. The gray vertical lines in (a, c) and (b, d) represent the longitudinal and latitudinal range of the research
731 domain of EAMBZ, respectively. The black shading indicates the topography. All variables are detrended and 11-year low-pass filtered.
732 Areas with significant values exceeding the 95% confidence level are stippled. The I_{EAMBZ} and I_{IOBM} /IPO index are calculated based
733 on the CRU TS3.26 precipitation data and the ERSSTv5 dataset, respectively; whilst other variables are from the 20CRv2c datasets.

734

735

736

737

738

739

740

741

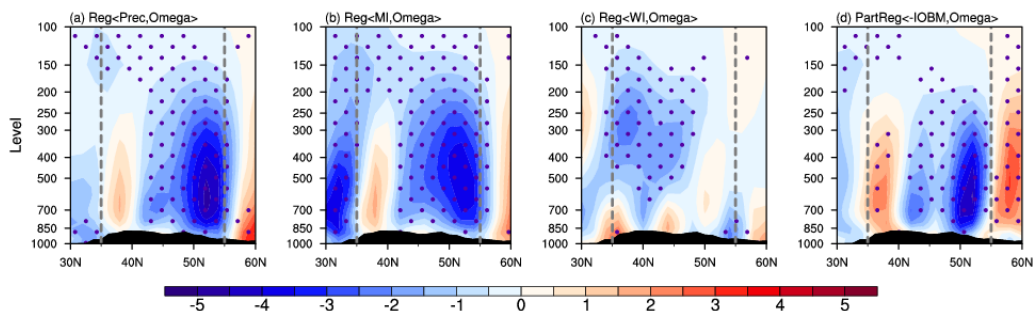
742

743

744

745

746



747

748 **Figure 5.** Height–latitude cross-section (averaged over 105°E – 130°E) of the JJA-mean vertical velocity anomalies (10^{-3}Pa s^{-1}) regressed
749 onto the concurrent (a) I_{EAMBZP} , (b) I_{MI} , and (c) I_{WI} during the period 1901–2014. (d) As in (a), but for the partial regressed anomalies
750 onto the negative I_{IOBM} with the IPO signal removed. The gray vertical lines represent the latitudinal range of EAMBZ. The black
751 shading indicates the topography. All variables are detrended and 11-year low-pass filtered. Areas with significant values exceeding
752 the 95% confidence level are stippled. The I_{EAMBZP} and $I_{\text{IOBM/IPO}}$ index are calculated based on the CRU TS3.26 precipitation data
753 and the ERSSTv5 dataset, respectively; whilst other variables are from the 20CRv2c datasets.

754

755

756

757

758

759

760

761

762

763

764

765

766

767

768

769

770

771

772

773

774

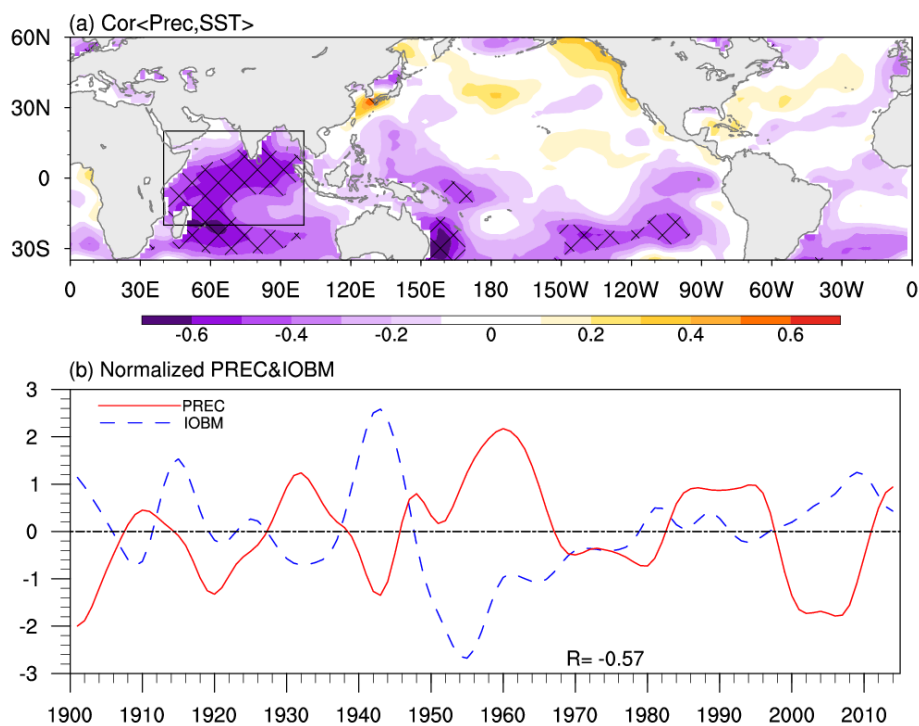
775

776

777

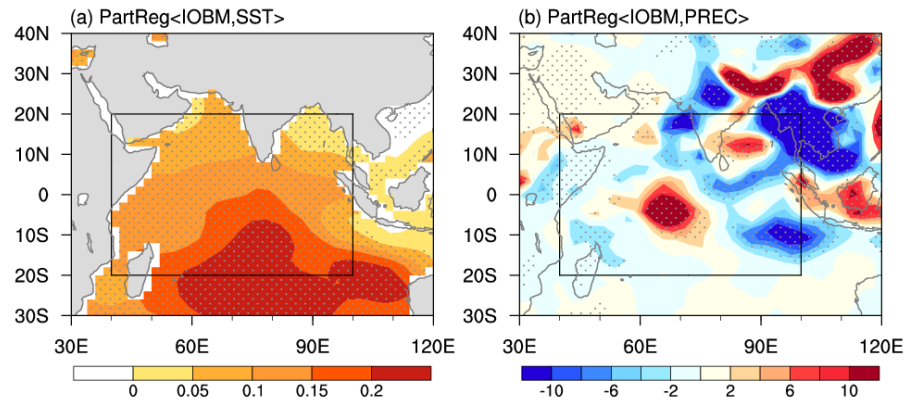
778

779



780
781 **Figure 6.** (a) Correlation map of the JJA-mean I_{EAMBZP} with the concurrent near-global SST (35°S–60°N) during the period 1901–
782 2014. The black frame (20°S–20°N, 40°E–100°E) outlines the domain for delineating the IOBM mode (the same hereinafter). Areas
783 with significant values exceeding the 99% confidence level are hatched. (b) Normalized time series of the JJA-mean I_{EAMBZP} (red line)
784 and I_{IOBM} (blue line) from 1901 to 2014. The numeral at the bottom represents the TCC between the corresponding time series. All
785 variables are detrended and 11-year low-pass filtered. The SST is from the ERSSTv5 dataset. The I_{EAMBZP} and I_{IOBM} are calculated
786 based on the CRU TS3.26 precipitation data and the ERSSTv5 datasets, respectively.

787
788
789
790
791
792
793
794
795
796
797
798
799



800

801 **Figure 7.** Partial regression of the JJA-mean (a) SST ($^{\circ}\text{C}$) and (b) precipitation (mm month^{-1}) anomalies over TIO and its neighboring
802 areas onto the concurrent I_{IOBM} with the IPO signal removed for the period 1901–2014. All variables are detrended and 11-year low-
803 pass filtered. Areas with significant values exceeding the 95% confidence level are stippled. The I_{IOBM} /IPO index is calculated based
804 on the ERSSTv5 dataset. The SST and the precipitation are derived from the ERSSTv5 dataset and the 20CRv2c dataset, respectively.

805

806

807

808

809

810

811

812

813

814

815

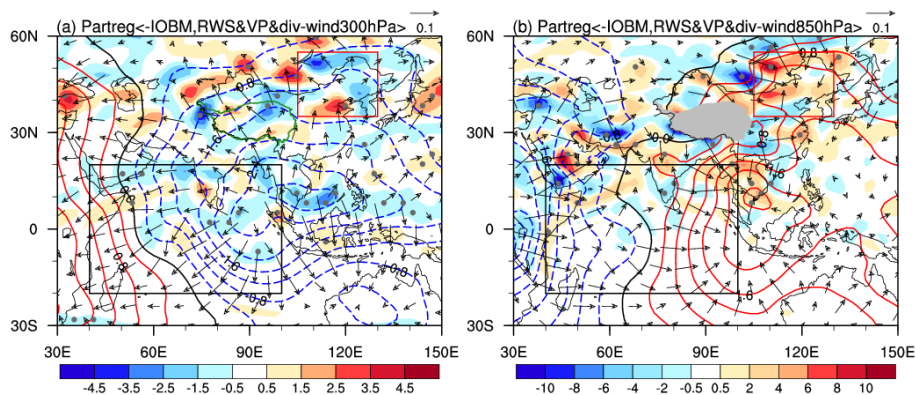
816

817

818

819

820



821

822 **Figure 8.** Partial regression of the JJA-mean (a) 300- and (b) 850-hPa RWS (shading; 10^{-11} s^{-2}), velocity potential (contours; interval:
823 $0.4; 10^5 \text{ m}^2 \text{ s}^{-1}$), and divergent horizontal wind (vectors; m s^{-1}) anomalies against the concurrent negative I_{IOBM} with the IPO signal
824 removed during the period 1901–2014. All variables are detrended and 11-year low-pass filtered. Areas with significant values of RWS
825 exceeding the 95% confidence level are stippled. The I_{IOBM} /IPO index is calculated based on the ERSSTv5 dataset; whilst other
826 variables are from the 20CRv2c datasets.

827

828

829

830

831

832

833

834

835

836

837

838

839

840

841

842

843

844

845

846

847

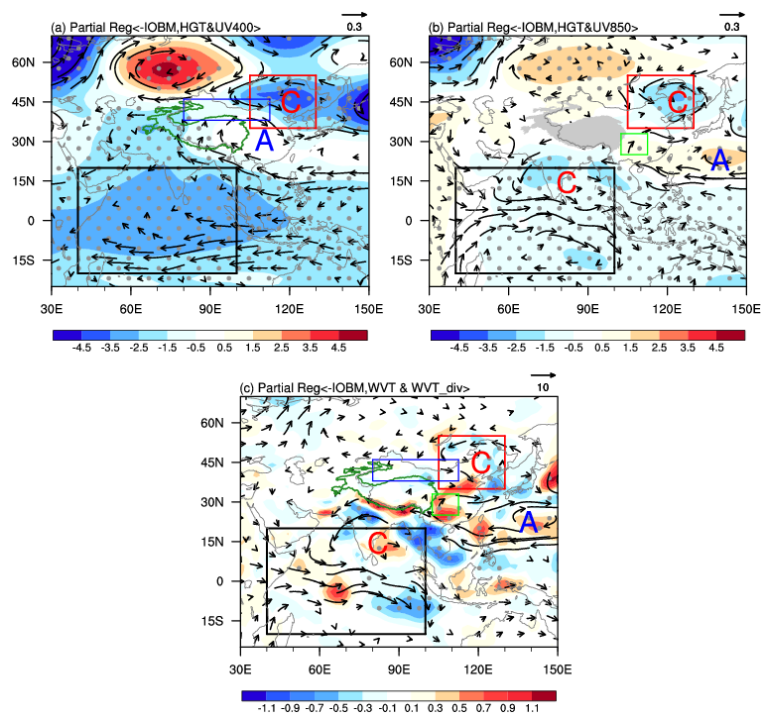
848

849

850

851

852



853

854 **Figure 9.** Partial regression of the JJA-mean (a) Z400 (shading; m) and UV400 (vectors; m s^{-1}), (b) Z850 (shading; m) and UV850
855 (vectors; m s^{-1}), and (c) $\langle \text{WVT} \rangle$ (vectors; $\text{kg m}^{-1} \text{s}^{-1}$) and $\langle \text{WVT}_{\text{div}} \rangle$ (shading; $10^{-5} \text{kg m}^{-2} \text{s}^{-1}$) onto the concurrent negative I_{IOBM}
856 with the IPO signal removed during the period 1901–2014. All variables are detrended and 11-year low-pass filtered. Areas with
857 significant values of Z400, Z850, and $\langle \text{WVT}_{\text{div}} \rangle$ that exceed the 95% confidence level are stippled, respectively. Only vectors that
858 are significant at the 95% confidence level are shown. The I_{IOBM} /IPO index is calculated based on the ERSSTv5 dataset; whilst other
859 variables are from the 20CRv2c datasets.

860

861

862

863

864

865

866

867

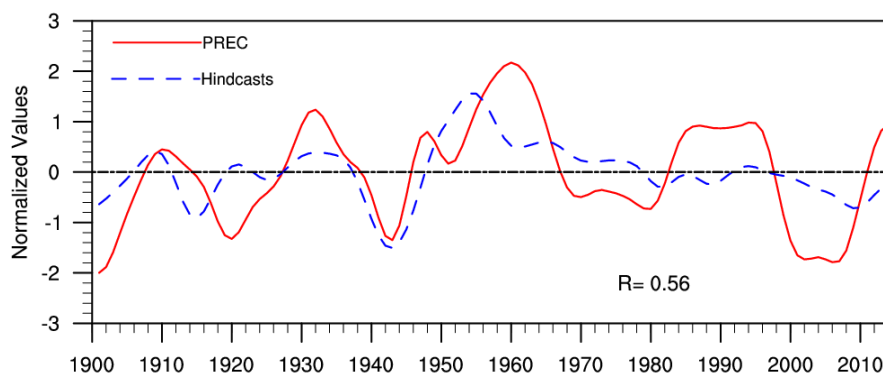
868

869

870

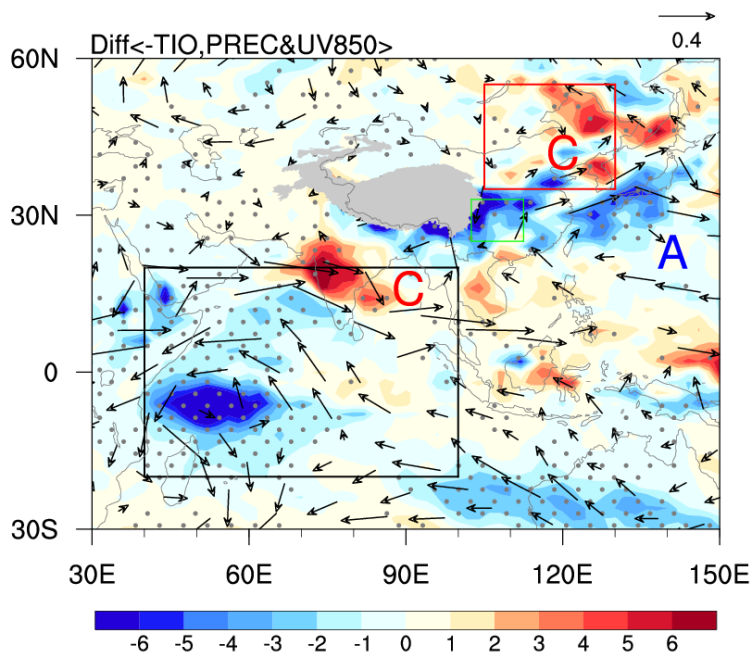
871

872



873
874 **Figure 10.** Normalized time series of the JJA-mean I_{EAMBZP} (red line) and associated leave-one-out cross-validated hindcast estimates
875 (blue line) for 1901–2014, with the number denoting the TCC between the corresponding time series.

876
877
878
879
880
881
882
883
884
885
886
887
888
889
890
891
892
893
894
895
896
897
898
899
900
901
902
903
904
905



906

907 **Figure 11.** Simulated composite differences of JJA-mean UV850 (vectors; m s^{-1}) and precipitation (shading; mm month^{-1}) between
908 cold and warm SST years over the broader TIO domain in CESM1_IOPES (15°S – 15°N , 40° – 174°E ; purple box in Fig. S4). The warm
909 and cold TIO SST years are selected based on the ± 0.5 standard deviations of the simulated time-evolving SSTAs during 1920–2005,
910 as shown in Fig. S3 (red line). All variables are detrended and 11-year low-pass filtered. Areas with significant values of precipitation
911 that exceed the 95% confidence level are stippled. Only vectors that are significant at the 95% confidence level are shown. The
912 simulated anomalies of UV850 and precipitation are calculated based on the difference between the CESM1_IOPES ensemble mean
913 and the CESM1_LENS ensemble mean (former minus latter), highlighting the internally driven impacts of TIO SSTAs.
914